Publication P3

Kristjan Tabri, Petri Varsta, and Jerzy Matusiak. 2010. Numerical and experimental motion simulations of nonsymmetric ship collisions. Journal of Marine Science and Technology, volume 15, number 1, pages 87-101.

J Mar Sci Technol (2010) 15:87–101
DOI 10.1007/s00773-009-0073-2

ORIGINAL ARTICLE

Numerical and experimental motion simulations of nonsymmetric ship collisions

Kristjan Tabri · Petri Varsta · Jerzy Matusiak

Received: 13 January 2009 / Accepted: 12 October 2009 / Published online: 12 November 2009

Abstract A calculation model to simulate nonsymmetric ship collisions, implying an arbitrary impact location and collision angle, is described in the paper. The model that is introduced is based on the time integration of twelve equations of motion, six for each ship. The motions of the ships are linked together by a mutual contact force. The contact force is evaluated as an integral over the surface tractions at the contact interface. The calculation model provides full time histories of the ship motions and the acting forces. Physical understanding of the underlying phenomena was obtained by a series of model-scale experiments in which a striking ship collided with an initially motionless struck ship. In this paper, numerical simulations of four nonsymmetric collisions are presented and the calculations are validated with the results of the experiments.

Keywords Collision dynamics · Nonsymmetric ship collisions · Model-scale collision experiments · Time domain simulation model

1 Introduction

Ship collisions continue to occur despite the development of numerous preventive measures. Human error, technical failures, and other unpredictable events can never be completely avoided. Eliopoulou and Papanikolaou [1] studied the statistics of tanker accidents and revealed that the total number of accidents and the number of accidents causing pollution has decreased significantly in recent decades. However, the accidents causing pollution have not decreased to the same extent as the overall number of accidents. It has become obvious that the measures applied to reduce the consequences of collisions should be improved, together with the preventive ones. To reduce the consequences, one has to understand the nature and the character of the underlying phenomena. A statistical study by Tuovinen [2] analysed more than 500 collision accidents, the data on which were gathered from published investigation reports, the IMO, database and damage cards. The statistical data presented the current trends, as the majority of the accidents studied (388) were registered during or after the year 1997, and only 115 accidents were registered before that. The study revealed that, with respect to the collision angle, only about every fourth collision can be considered symmetric, i.e. the striking ship collides with the amidships of the struck ship at right angles. In the studied cases, about 25% of the collisions occurred at a right angle or in its vicinity ($\pm 10°$). All of the other accidents were in one way or another considered to be nonsymmetric. This fact emphasises the importance of understanding the nature of nonsymmetric collisions. Thus, this paper is focused on the physical phenomena of nonsymmetric ship collisions, and a calculation model is proposed to predict the ship motions and the structural damage in such a collision.

Several calculation models for simulating the dynamics of ship collisions exist. The calculation models can be classified as closed form expressions or as time domain simulations. Closed form models are based on the conservation of momentum and allow a fast estimation of structural deformation energy without providing the time histories of ship motions, which leaves the exact penetration

K. Tabri (✉) · P. Varsta · J. Matusiak
Department of Applied Mechanics, Marine Technology,
Helsinki University of Technology,
P.O. Box 5300, 02015 TKK, Espoo, Finland
e-mail: kristjan.tabri@tkk.fi

path of the colliding bodies unknown. In closed form models, there is no coupling between the external dynamics and the inner mechanics, and therefore no coupling effects are included. One of the first closed form models for ship collisions for a single degree of freedom (*dof*) was proposed by Minorsky [3]. This model has been modified and extended by many authors to consider up to three *dof* in the horizontal plane [4, 5].

In time domain simulation models, the system of equations of ship motion is solved using a numerical integration procedure. A precise description of the whole collision process, together with the full time histories of the motions and forces involved, is achieved. Motion-dependent forces, such as the radiation forces arising from the interaction with the surrounding water, can be included in the analysis. As a result of the complexity involved in solving the equations, these simulation models are often reduced to include the motions in the horizontal plane only [6, 7].

The proposed calculation model is based on a time domain simulation that takes into account six *dof* for each ship and is thus capable of handling arbitrary collision angles and locations. The inner mechanics and the external dynamics are coupled, preserving the interaction between the colliding ships, which makes it possible to estimate the time history of the common contact force. This force is evaluated by considering the geometry of the colliding ships and calculating the surface tractions at the contact interface. The striking ship is assumed to be rigid, and all of the structural deformations are limited to the struck ship. The calculation model that is developed aims to predict the ship motions until the contact between the ships is lost. This requires precise modelling of the effects of the surrounding water, and the popular approach of using constant added mass as a representative of the radiation force does not suffice; thus, in addition, the retardation functions [8, 9] are used to include the time dependency of the radiation force. The model adopts a linear approach to the restoring force, limiting the angular displacements from the equilibrium position to small angles, i.e. below 10°. More accurate methods, such as the precise integration of hydrostatic pressure over the ship's hull, allow larger displacements and angles, but the integration process is very time-consuming and therefore is not considered here. Frictional water resistance and hydrodynamic drag are assumed to be proportional to the square of the ship's velocity. Effects arising from the wave pattern around the colliding ships and from the immediate consequences of the collision, such as flooding and loss of stability, are not included in the calculation model.

The physical phenomena are studied and the calculations are validated with non-symmetric model-scale collision experiments. The test setup for the experiments was designed and validated with large-scale collision tests [10]. The emphasis in the model tests was placed on the external dynamics, and thus the side structure of the struck ship was modelled using polyurethane foam. The scaling of the contact force was based on the results of the large-scale experiments. During the collision, the motions of both ships in all six *dof* were measured, as was the contact force in the longitudinal and the transverse directions with respect to the striking ship. Several collision scenarios, with different collision angles and locations, were tested in order to obtain not only large translational motions but also relatively large angular motions. The tests were limited to those cases where the striking ship approaches an initially motionless struck ship. This was mainly due to the test setup of the model tests, where the focus was on the physical phenomena. In all of the tests, the contact point on the struck ship was above the waterline and was located in the parallel middle body.

2 Calculation model

The calculation model assumes a situation in which the rigid striking ship approaches, at a certain angle, a specific location on the struck ship. As soon as the ships are brought into contact, the contact force starts to play a major role in the collision dynamics. When the contact is lost, the force decreases to zero and the hydromechanical forces will govern the collision process. The equilibrium between the forces acting on the ship and the resultant ship motions is described through a system of six equations of motion. These Newtonian equations are expressed in a local coordinate system of the ship, allowing convenient description of the hydromechanical forces. The numerical time integration of these equations yields the ship motions in the local coordinate system. Though the motions are conveniently presented in the local frames, the position and orientation of the ships can only be specified by reference to an inertial coordinate system that is fixed with respect to the Earth.

2.1 Motion kinematics

The convenient description of the mutual motions and the kinematic connection of the colliding bodies requires five different coordinate systems, which are presented in Fig. 1. Hereafter, the superscript characters A and B denote the striking and the struck ship, respectively. If the superscript is omitted or replaced by i, it means that the description is common to both ships. Superscript 0 indicates the inertial frame. The origins O^i of two sets of local axes are fixed to the mass centre of gravity of the ship. Positioning the coordinate systems at the centre of gravity simplifies the analysis, as the acceleration components resulting from mass eccentricity disappear. For ship position, reference is

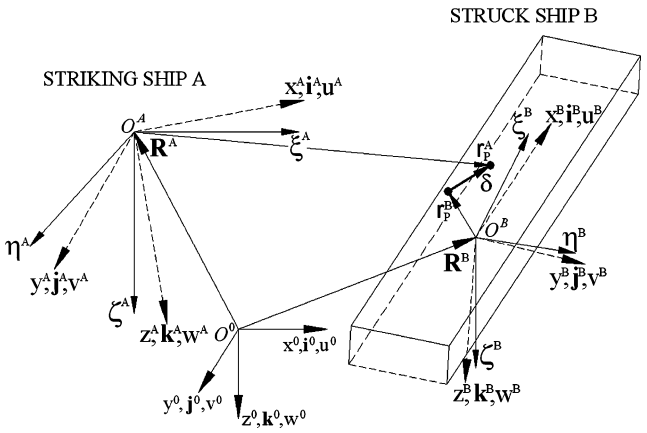

Fig. 1 Definition of coordinate systems and position vectors

made to the inertial coordinate system $O^0x^0y^0z^0$ with a position vector $\mathbf{R}^i$, but when describing the ship motions it is common to refer in the local coordinate system to surge, sway, heave, roll, pitch, and yaw. The first three are translations along the axes and the last are rotational motions. The instantaneous translational velocity $\mathbf{u}^i$ of the ship's centre of gravity is given as a time derivative of the position vector $\mathbf{R}^i$

$$\mathbf{u}^i = \dot{\mathbf{R}}^i = \dot{x}^0\mathbf{i}^0 + \dot{y}^0\mathbf{j}^0 + \dot{z}^0\mathbf{k}^0 = u^i\mathbf{i}^i + v^i\mathbf{j}^i + w^i\mathbf{k}^i \tag{1}$$

where $\dot{x}^0$, $\dot{y}^0$ and $\dot{z}^0$ are the velocities of the ship's centre of gravity in the inertial frame and u, v and w are their projections onto the local coordinate system $O^ix^iy^iz^i$.

The second set of local axes, referred to as the horizontal body axes $O^i\xi^i\eta^i\zeta^i$, are used for a more convenient presentation of the orientation of the ships. At the onset of the contact process, the directions of the $O^A\xi^A\eta^A\zeta^A$ system coincide with those of the inertial frame $O^0x^0y^0z^0$, while $O^B\xi^B\eta^B\zeta^B$ is rotated with respect to $O^0x^0y^0z^0$ to obtain the collision angle β. The collision angle β is defined as the angle between $\mathbf{i}^0$ and the direction of ξ^B. The positions of $O^A\xi^A\eta^A\zeta^A$ and $O^B\xi^B\eta^B\zeta^B$ at the onset of the contact are considered to be the reference positions of the ships. Both sets of local axes, $O^i\xi^i\eta^i\zeta^i$ and $O^ix^iy^iz^i$, are coincident at the beginning of the contact. During the calculation, these horizontal body axes are only subjected to translational motions, and the body fixed coordinate system $O^ix^iy^iz^i$ is reoriented with respect to $O^i\xi^i\eta^i\zeta^i$.

The orientation of the ship is defined using the method of modified Euler angles [11]. In this method, the rotations must be handled in a certain order: first a "swing" ψ to the actual azimuth, then a "tilt" θ to the actual elevation, and finally a "heel" ϕ to the actual orientation. The relation between the velocities in the inertial coordinate system and their projections onto the local axis is given [11] by an orthogonal matrix of transformation [**T**]:

$$\begin{Bmatrix} \dot{x}^0 \\ \dot{y}^0 \\ \dot{z}^0 \end{Bmatrix} = [\mathbf{T}] \begin{Bmatrix} u^i \\ v^i \\ w^i \end{Bmatrix}$$

$$= \begin{bmatrix} \cos\psi\cos\theta & \cos\psi\sin\theta\sin\phi - \sin\psi\cos\phi & \cos\psi\sin\theta\cos\phi + \sin\psi\sin\phi \\ \sin\psi\cos\theta & \sin\psi\sin\theta\sin\phi + \cos\psi\cos\phi & \sin\psi\sin\theta\cos\phi - \cos\psi\sin\phi \\ -\sin\theta & \cos\theta\sin\phi & \cos\theta\cos\phi \end{bmatrix} \times \begin{Bmatrix} u^i \\ v^i \\ w^i \end{Bmatrix} \tag{2}$$

Matrices are denoted by [] and vectors by {} in equations where both types of objects are present. In equations consisting only of vectors, or when the actual type is obvious, the above notation in omitted for the sake of brevity. Position and force vectors can be transformed in a similar manner as the velocities in Eq. 2. The angular velocity $\mathbf{\Omega}^i$ is defined in the local coordinate system as

$$\mathbf{\Omega}^i = p^i\mathbf{i}^i + q^i\mathbf{j}^i + r^i\mathbf{k}^i \tag{3}$$

where p^i, q^i, and r^i are the angular rates of roll, pitch, and yaw in the local coordinate system. The derivatives of the Euler angles depend on the angular rates as [11]

$$\begin{Bmatrix} \dot{\phi} \\ \dot{\theta} \\ \dot{\psi} \end{Bmatrix} = \begin{bmatrix} 1 & \sin\phi\tan\theta & \cos\phi\tan\theta \\ 0 & \cos\phi & -\sin\phi \\ 0 & \sin\phi/\cos\theta & \cos\phi/\cos\theta \end{bmatrix} \begin{Bmatrix} p^i \\ q^i \\ r^i \end{Bmatrix} \tag{4}$$

It should be noted that even though the angular rates $\dot{\phi}$, $\dot{\theta}$, and $\dot{\psi}$ are vector quantities, the Euler angles cannot be presented as a vector. For the sake of simplicity, they are still collectively referred to via a column matrix $[\varphi] = [\,\phi \quad \theta \quad \psi\,]^{\mathrm{T}}$.

The translational velocity $\mathbf{u}_P^i$ of a point P positioned by the vector $\mathbf{r}_P^i$ in the local coordinate system is evaluated as

$$\mathbf{u}_P^i = \mathbf{u}^i + \mathbf{\Omega}^i \times \mathbf{r}_P^i \tag{5}$$

The relative position between the ships is described by a penetration vector $\boldsymbol{\delta}$ that is defined in the inertial frame as

$$\boldsymbol{\delta}^0 = \mathbf{R}^A + \mathbf{r}_P^A - \left(\mathbf{R}^B + \mathbf{r}_P^B\right) \tag{6}$$

It is also useful to express this penetration in the body fixed coordinate systems to account for the orientation of the ships:

$$\boldsymbol{\delta}^A = \boldsymbol{\delta}^0 \cdot \mathbf{i}^A + \boldsymbol{\delta}^0 \cdot \mathbf{j}^A + \boldsymbol{\delta}^0 \cdot \mathbf{k}^A \tag{7}$$

$$\boldsymbol{\delta}^B = \boldsymbol{\delta}^0 \cdot \mathbf{i}^B + \boldsymbol{\delta}^0 \cdot \mathbf{j}^B + \boldsymbol{\delta}^0 \cdot \mathbf{k}^B \tag{8}$$

2.2 Fluid forces and gravity

Hydromechanical forces and moments acting on a surface ship consist of water resistance, hydrostatic restoring forces, and radiation forces expressed in terms of hydrodynamic damping and added mass. A ship moving in water encounters frictional and residual resistance. Residual resistance is not included in the study because it is considered to be small compared to other phenomena. The frictional water resistance is considered only for surge and sway. The friction force $F_{\mathrm{F},x}$ for surge is approximated with the ITTC-57 friction line formula. For sway, the hydrodynamic drag force $F_{\mathrm{F},y}$ is calculated as [12]

$$F_{\mathrm{F},y} = \frac{1}{2}\rho v^2 C_y A_{\mathrm{L}} \tag{9}$$

where ρ is the water density, v is the sway velocity, C_y is a drag coefficient that depends on the shape of the hull and on the angle between the ship's longitudinal axis and its velocity vector, and A_{L} is the lateral underwater area of the ship. In the model tests reported by Gale [12], it is shown that the drag coefficient C_y varies between 0.5 and 1.2, and $C_y = 1$ is used in the subsequent calculations.

Buoyancy loading $\mathbf{F}_{\mathrm{B}}$ is split into the buoyancy $\rho g \nabla \mathbf{k}^0$ at the equilibrium position and the hydrostatic restoring force $\mathbf{F}_{\mathrm{R}}$:

$$\mathbf{F}_{\mathrm{B}} = -\rho g \nabla \mathbf{k}^0 + \mathbf{F}_{\mathrm{R}} = -\rho g \nabla \mathbf{k}^0 + [\mathbf{K}] \begin{Bmatrix} \{\mathbf{x}\} \\ [\boldsymbol{\varphi}] \end{Bmatrix} \tag{10}$$

where g is the gravitational acceleration, ∇ is the volumetric displacement of the ship, $[\mathbf{K}]$ is a matrix of linear restoring terms, $\{\mathbf{x}\}$ presents a vector of translational displacements from the equilibrium position, and $[\boldsymbol{\varphi}]$ are the Euler angles already described in the previous section. The terms of the matrix $[\mathbf{K}]$ are presented in Appendix 1. As these restoring terms are based on small angular displacements, the same linear restoring terms can be applied both in the local and the inertial coordinate systems. Gravity loading $\mathbf{F}_{\mathrm{G}}$ opposes the buoyancy in the equilibrium position:

$$\mathbf{F}_{\mathrm{G}} = \rho g \nabla \mathbf{k}^0 \tag{11}$$

It is common practice to model the radiation forces by frequency-dependent added mass $a(\omega)$ and damping $b(\omega)$ coefficients. To represent the radiation forces in the time domain, it is useful to split them into a part $\mathbf{F}_{\mu}$ proportional to the acceleration and into a velocity-dependent damping part $\mathbf{F}_{\mathrm{K}}$: [8]

$$\mathbf{F}_{\mu}(t) + \mathbf{F}_{\mathrm{K}}(t) = -[\boldsymbol{a}_{\infty}] \begin{Bmatrix} \dot{\mathbf{u}}(t) \\ \dot{\boldsymbol{\Omega}}(t) \end{Bmatrix} - \int_0^t [\mathbf{K}_b(\tau)] \begin{Bmatrix} \mathbf{u}(t-\tau) \\ \boldsymbol{\Omega}(t-\tau) \end{Bmatrix} \mathrm{d}\tau \tag{12}$$

where t denotes time, τ is a dummy variable, $[\boldsymbol{a}_{\infty}]$ is the matrix of added masses $a(\omega = \infty)$ at infinite frequency, and $[\mathbf{K}_b(\tau)]$ is a matrix of retardation functions, which account for the memory effect:

$$[\mathbf{K}_b(\tau)] = \frac{2}{\pi} \int_0^{\infty} [\mathbf{b}(\omega)] \cos(\omega\tau)\, \mathrm{d}\omega \tag{13}$$

where $[\mathbf{b}(\omega)]$ is a matrix comprising of added damping terms. The retardation functions $K_b(\tau)$ are evaluated by fast Fourier transformation [13].

2.3 Contact process between ships

During a collision, the ships interact through the contact force arising from the deformations of their structures. The interaction model presented in this chapter considers a homogeneous side structure whose stiffness is significantly lower than that of the striking ship. Thus, it is reasonable to assume that all of the deformations are limited to the struck ship and that the striking ship can be treated as rigid. The deformed shape of the side structure of the struck ship is restricted to following the shape of the penetrating bow. Throughout the derivation of the contact model it is assumed that the stress state in the deformed structures can be obtained easily, and so the derivation of the contact force concentrates on the contact kinematics.

When two nonconforming bodies are brought into contact, they initially touch each other at a single point or line. As the contact proceeds and the bow penetrates further into the struck ship, the contact interface expands. To predict the shape of the contact interface—see Fig. 2—the geometries of the colliding bodies are defined in the local coordinate system of the striking ship. Therefore, the surface $\mathcal{S}$ of the axisymmetric bulbous bow of the striking ship is defined as

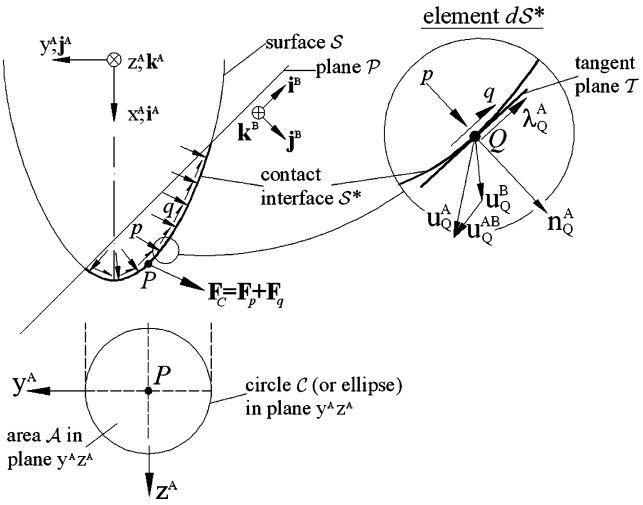

Fig. 2 Contact geometry with kinematics and surface tractions

$$x^A = f^A\left(a, b, c, y^A, z^A\right) \tag{14}$$

where a, b, and c are the shape parameters. It is assumed that Eq. 14 has first-order partial derivatives inside the contact interface. The geometry, position, and orientation of the struck ship B are transferred to $O^A x^A y^A z^A$ and are approximated as a plane $\mathcal{P}$ by

$$x^A = f^B\left(A, B, C, y^A, z^A\right) \tag{15}$$

where A, B, and C are the parameters defining the plane. Subtracting Eq. 15 from Eq. 14 yields the curve $\mathcal{C}$ of intersection that bounds the contact interface $\mathcal{S}^*$ in the $y^A z^A$ plane; see Fig. 2. The area bounded by curve $\mathcal{C}$ is denoted as area $\mathcal{A}$. Contact between the ships exists when curve $\mathcal{C}$ exists and thus area $\mathcal{A}$ has a real positive value.

The magnitude and the direction of the contact force $\mathbf{F}_C$ depend on the structural geometry and on the relative motions of the colliding ships. As the bow penetrates into the side structure, surface tractions are formed on the contact interface. The normal traction—referred to as pressure—is denoted by p and the tangential traction caused by friction by q in Fig. 2.

The resultant contact force $\mathbf{F}_C$ is resolved into a compressive part $\mathbf{F}_p$ and a frictional part $\mathbf{F}_q$. It is assumed that this resultant force acts at point P, which is the centre of area $\mathcal{A}$. At the exact centre of the contact, the resultant moment of surface tractions is zero. Even though this condition is not always satisfied at point P, it is still used as the centre. The moment lever that is caused is considered small compared to the dimensions of the ship, and thus the additional moment is neglected.

2.3.1 Compressive and friction force

Inside the contact interface $\mathcal{S}^*$, every infinitesimal area dS* described by its central point Q in the right-hand picture in Fig. 2 is subjected to normal compressive traction p and to tangential traction q. The force resulting from the normal traction is evaluated by integrating over the interface $\mathcal{S}^*$

$$\mathbf{F}_p^A = \iint_{S^*} p\mathbf{n}_Q^A \, \mathrm{d}S^* \tag{16}$$

where $\mathbf{n}_Q^A$ is an unit normal at Q pointing outside the bulb, and is defined as

$$\mathbf{n}_Q^A = \frac{\left(\mathbf{i} - \frac{\partial f^A}{\partial y^A}\mathbf{j} - \frac{\partial f^A}{\partial z^A}\mathbf{k}\right)}{\sqrt{1 + \left(\frac{\partial f^A}{\partial y^A}\right)^2 + \left(\frac{\partial f^A}{\partial z^A}\right)^2}} \tag{17}$$

The surface integral over $\mathcal{S}^*$ can be expressed as a more convenient integral over area $\mathcal{A}$:

$$\iint_{S^*} \mathrm{d}S^* = \iint_{\mathcal{A}} \sqrt{1 + \left(\frac{\partial f^A}{\partial y^A}\right)^2 + \left(\frac{\partial f^A}{\partial z^A}\right)^2} \, \mathrm{d}y^A \, \mathrm{d}z^A \tag{18}$$

The bulb geometry and the distribution of p in the contact interface define the direction of $\mathbf{F}_p^A$. The frictional force component $\mathbf{F}_q$ acts on a tangent plane $\mathcal{T}$ at point Q; see Fig. 2. The direction of this force is denoted by the vector $\boldsymbol{\lambda}_Q^A$ and it depends on the contact kinematics. The discussion about the exact value of $\boldsymbol{\lambda}_Q^A$ is presented in the next section. Assuming that the tangential traction is proportional to the pressure, the frictional force can be evaluated as

$$\mathbf{F}_q^A = \iint_{S^*} q\boldsymbol{\lambda}_Q^A \, \mathrm{d}S^* = \iint_{S^*} \mu_q p\boldsymbol{\lambda}_Q^A \, \mathrm{d}S^* \tag{19}$$

where μ_q is the coefficient of friction. The resultant contact force acting on point P is

$$\mathbf{F}_C^A = -\mathbf{F}_C^B = \mathbf{F}_p^A + \mathbf{F}_q^A \tag{20}$$

Within the loaded interface at any point Q, there is equilibrium between the normal traction and the stresses in the deformed material at the contact interface:

$$p = -\sigma_n \tag{21}$$

where σ_n indicates the normal stresses in the direction of the surface normal.

2.3.2 Contact phases

The contact process is divided into three distinct phases. The contact starts with the loading phase, during which the penetration increases. The loading is followed by a short stiction phase, during which the penetration remains roughly the same. The contact process ends with the unloading phase, during which the penetration decreases as a result of the separation of the ships. All three phases differ with respect to contact kinematics, which is defined by the relative velocity between the ships at the integration point Q

$$\mathbf{u}_Q^{AB} = \mathbf{u}_Q^A - \mathbf{u}_Q^B \tag{22}$$

and additionally by the relative acceleration $\dot{\mathbf{u}}_Q^{AB}$. An integration element d$\mathcal{S}^*$, presented in Fig. 2, is assumed to undergo the loading phase when the following three conditions are fulfilled:

1. The angle between $\mathbf{u}_Q^{AB}$ and $\mathbf{n}_Q^A$ is less than 90°
2. The magnitude $|\mathbf{u}_Q^{AB}|$ is larger than the threshold velocity u_0^{AB}
3. The penetration with respect to the transverse direction of the struck ship is increasing, i.e. $\mathbf{u}_Q^{AB} \cdot \mathbf{j}^B > 0$.

In the loading phase, the direction of $\boldsymbol{\lambda}_Q^A$ opposes the projection of the relative velocity $\mathbf{u}_Q^{AB}$ to the tangent plane $\mathcal{T}$ of the indenter, and is defined as

$$\boldsymbol{\lambda}_Q^A = -\mathrm{proj}_{\mathcal{T}} \frac{\mathbf{u}_Q^{AB}}{\left|\mathbf{u}_Q^{AB}\right|} \tag{23}$$

where $\mathrm{proj}_{\mathcal{T}}\mathbf{u}$ indicates the projection of a vector $\mathbf{u}$ onto the plane $\mathcal{T}$, and can be written as

$$\mathrm{proj}_{\mathcal{T}}\mathbf{u} = \mathbf{n} \times (\mathbf{u} \times \mathbf{n}) \tag{24}$$

where $\mathbf{n}$ is the unit normal vector of the plane.

During the transition phase from the loading to the unloading, the angle between $\mathbf{u}_Q^{AB}$ and $\mathbf{n}_Q^A$ increases and becomes larger than 90°. If during this transition the magnitude $|\mathbf{u}_Q^{AB}|$ falls below the threshold velocity u_0^{AB}, the integration element $\mathrm{d}\mathcal{S}^*$ undergoes the stiction phase. Figure 3a presents a situation in which a surface element close to the boundary of the contact interface is in the stiction phase. The time instant when the first surface element enters either the stiction or the unloading phase is denoted as $t = t_{e1}$.

In the stiction phase, $\mathbf{u}_Q^{AB}$ approaches zero and possibly changes its sign. Therefore, evaluating the direction of $\boldsymbol{\lambda}_Q^A$ by the relative velocity $\mathbf{u}_Q^{AB}$ may yield the singularity problem in Eq. 23. Despite the small relative velocity, the friction or (more properly) the stiction force does not disappear, as the bodies—even though they are not sliding—still undergo small reversible elastic deformations that result in an interaction force [14]. In order to avoid using complicated theoretical models for stiction, the proportional friction is still used, but the direction is based on the relative acceleration $\dot{\mathbf{u}}_Q^{AB}$ at Q, as suggested by several authors [14, 15], and thus the direction of $\boldsymbol{\lambda}_Q^A$ is defined as

$$\boldsymbol{\lambda}_Q^A = -\mathrm{proj}_{\mathcal{T}} \frac{\dot{\mathbf{u}}_Q^{AB}}{\left|\dot{\mathbf{u}}_Q^{AB}\right|} \tag{25}$$

In the unloading phase, either (1) or (3) or both conditions are not satisfied. When the penetration starts to decrease, the contact is not immediately lost as a result of the elasticity of the structures. The deformation of the structure recovers to some extent in order to restore its initial undeformed shape. This elastically recovered region is simply referred to as the recovered region. It is assumed that the structure recovers along the shortest possible path, i.e. along $-\mathbf{j}^B$. The final shape of the recovered region follows the surface geometry of the penetrating bow. The amount of restoration is controlled by the relative thickness of the recovered region ε and by the transverse penetration $\boldsymbol{\delta}^0 \cdot \mathbf{j}^B$ in the struck ship. The shape of the elastic region is given in a general form as

$$x^A = f^{\varepsilon}(a, b, c, \varepsilon, \boldsymbol{\delta}^0 \cdot \mathbf{j}^B, y^A, z^A) \tag{26}$$

In Sect. 3.2, the functions f^A, f^B, f^{ε} given by Eqs. 14, 15, and 26, the parameters a, b, c, A, B, and C, and the material properties σ_n, μ_q, and ε are presented for the contact configurations used in the model-scale experiments.

In the unloading phase, the direction of $\boldsymbol{\lambda}_Q^A$ has to take into account the velocity of elastic recovery. As the recovering structure maintains the contact with the indenter, and as the

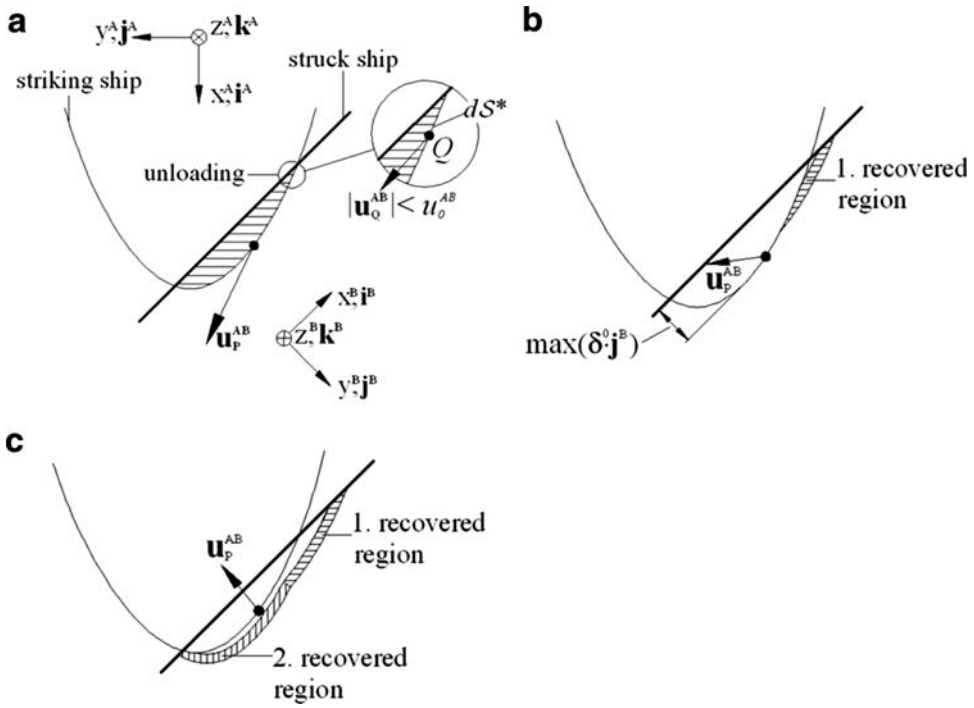

Fig. 3 Reversal of the velocity vector during the transition from the loading to the unloading phase and the storing of the elastic regions. **a** Stiction phase starts at $t = t_{e1}$. **b** Maximum penetration is reached at $t = t_{e2} > t_{e1}$. **c** Two recovered regions at $t = t_j > t_{e2} > t_{e1}$

recovery is along $-\mathbf{j}^B$, the velocity of the elastic recovery is $\left(\mathbf{u}_Q^{AB}\cdot\mathbf{j}^B\right)\mathbf{j}^B$, and thus the relative velocity between the de-penetrating bow and the recovering structure is

$$\mathbf{u}_Q^A-\left(\mathbf{u}_Q^B+\left(\mathbf{u}_Q^{AB}\cdot\mathbf{j}^B\right)\mathbf{j}^B\right)=\mathbf{u}_Q^{AB}-\left(\mathbf{u}_Q^{AB}\cdot\mathbf{j}^B\right)\mathbf{j}^B \tag{27}$$

and the direction $\boldsymbol{\lambda}_Q^A$ of the friction force is evaluated as

$$\boldsymbol{\lambda}_Q^A=-\mathrm{proj}_{\mathcal{T}}\left[\frac{\mathbf{u}_Q^{AB}-\left(\mathbf{u}_Q^{AB}\cdot\mathbf{j}^B\right)\mathbf{j}^B}{\left|\mathbf{u}_Q^{AB}-\left(\mathbf{u}_Q^{AB}\cdot\mathbf{j}^B\right)\mathbf{j}^B\right|}\right] \tag{28}$$

The recovered region is evaluated at two time instants, as indicated in Fig. 3: first at $t=t_{e1}$, when the stiction or the unloading phase occurs for the first time in some integration element, and for the second time at $t=t_{e2}$ when the transverse penetration $\boldsymbol{\delta}^0\cdot\mathbf{j}^B$ in the struck ship reaches its maximum value. The first region is always updated when the bow penetrates further. During later stages, when $t=t_j>t_{e2}$, at each integration point Q the recovered region is determined by the larger penetration value.

2.4 Equation of motion

A ship with its mass described in a mass matrix [**M**] and moments of inertia in an inertia matrix [**I**] is subjected to the external force

$$\mathbf{F}=\mathbf{F}_{\mathrm{F}}+\mathbf{F}_{\mu}+\mathbf{F}_{\mathrm{K}}+\mathbf{F}_{\mathrm{C}}+\mathbf{F}_{\mathrm{B}}+\mathbf{F}_{\mathrm{G}} \tag{29}$$

and to the moment **G** of the external force about the centre of gravity of the ship. All of the forces are described or transferred by the matrix [**T**] to the local coordinate system $O^ix^iy^iz^i$, where the general equation of translational motions is written according to Newton's law as [11]

$$[\mathbf{M}]\frac{\delta\mathbf{u}}{\delta t}+[\mathbf{M}]\boldsymbol{\Omega}\times\mathbf{u}=\mathbf{F} \tag{30}$$

and correspondingly for rotational motions as

$$[\mathbf{I}]\frac{\delta\boldsymbol{\Omega}}{\delta t}+\boldsymbol{\Omega}\times[\mathbf{I}]\boldsymbol{\Omega}=\mathbf{G} \tag{31}$$

The time integration of these equations is based on an explicit fifth-order Dormand–Prince integration scheme [16], which is a member of the Runge–Kutta family of solvers, where the calculation advances from t_j to $t_{j+1}=t_j+\mathrm{d}t$ with seven subincrements. For time-efficient integration, the forces on the right-hand side of the equations are kept constant during time step dt, while the motions on the left-hand side are updated in every subincrement. Thus, the preciseness of the integration can be increased by moving some force components from the right-hand side to the left. This is done with the forces that do not require history values from former time steps and are linear with respect to motions. Therefore, the hydrostatic restoring force $\mathbf{F}_{\mathrm{R}}$ proportional to the displacements and the radiation force component $\mathbf{F}_{\mu}$ are moved to the left. The latter results in a full added mass matrix containing several terms, which couple the translational and rotational motions. This fully coupled added mass matrix and the coupling term $\boldsymbol{\Omega}\times\mathbf{u}$ in Eq. 30 require the simultaneous solution of translational and rotational motions. In their general form, the two equations of motion are combined to give

$$\begin{bmatrix}[\mathbf{M}] & 0\\ 0 & [\mathbf{I}]\end{bmatrix}\begin{Bmatrix}\dot{\mathbf{u}}\\ \dot{\boldsymbol{\Omega}}\end{Bmatrix}+\begin{Bmatrix}[\mathbf{M}]\boldsymbol{\Omega}\times\mathbf{u}\\ \boldsymbol{\Omega}\times[\mathbf{I}]\boldsymbol{\Omega}\end{Bmatrix}-\mathbf{F}_{\mathrm{R}}-\mathbf{F}_{\mu}=\begin{Bmatrix}\mathbf{F}\\ \mathbf{G}\end{Bmatrix}-\mathbf{F}_{\mathrm{R}}-\mathbf{F}_{\mu} \tag{32}$$

and the component form of this equation that is suitable for numerical integration is presented in Appendix 1. The solution of Eq. 32 provides kinematically admissible motions at the end of the integration increment at $t=t_{j+1}$, and the external forces on the right-hand side are updated accordingly. There, the new position of the ship with respect to the inertial frame is evaluated by integrating with respect to time over the velocities in the local coordinate system and transforming the translational displacement increments that are obtained to the inertial frame by the matrix [**T**]. These increments are added to the position vector $\mathbf{R}^i$. The orientation is updated by simply adding the angular increments to the Euler angles. Given the positions and the orientations, the penetrations are calculated from Eqs. 6 to 8. The equations of motion, Eq. 32, are established for each ship. These equations are treated separately in the integration during the time increment dt, and after each step the mutual contact force $\mathbf{F}_{\mathrm{C}}^A=-\mathbf{F}_{\mathrm{C}}^B$ is updated for both ships in order to maintain the kinematic connection.

3 Model-scale experiments of ship collisions

The full-scale experiments [17] provided validation data for symmetric collisions in which the ship motions are limited to only a few components. In order to gain a deeper insight into the dynamics of nonsymmetric collisions, a series of model-scale experiments was performed at the Helsinki University of Technology. The model tests were designed to be physically similar to the large-scale experiments. The design, scaling, and validation of the test setup for the model-scale experiments are explained in detail by Tabri et al. [10] and Määttänen [18].

3.1 Test setup and measuring systems

The general arrangement of the test setup is presented in Fig. 4. The models were geometrically similar to the ships participating in the full-scale experiments. Considering the level of structural resistance of the ship models and the

dimensions of the test basin, the feasible scaling factor λ for the Froude scaling law was determined to be $\lambda = 35$. This resulted in models of length $L = 2.29$ m, depth $D = 0.12$ m, and breadth $B = 0.234$ m for the striking ship and $B = 0.271$ m for the struck ship.

Table 1 presents draughts, masses, the vertical height of the centre of gravity KG, and the radii of inertia k_{ii} for different loading conditions in the ship models. The longitudinal centre of gravity of the ships is always located at the amidships. The table also presents the values for the added masses. The nondimensional added mass coefficients μ are calculated as

$$\mu_j = \lim_{\omega\to\infty} \frac{a_j(\omega)}{\rho\nabla}, \text{ with } j = x, y, z \tag{33}$$

for translational motions such as sway and heave and

$$\mu_{jj} = \lim_{\omega\to\infty} \frac{a_{jj}(\omega)}{\rho\nabla k_{jj}^2}, \text{ with } j = x, y, z \tag{34}$$

for rotational motions such as roll, pitch, and yaw. The frequency-dependent added mass $a(\omega)$ was evaluated with strip theory [19]. The coefficients were first evaluated in a coordinate system with its origin located in the water plane. As the equations of motion are established in the $O^i x^i y^i z^i$ system, the origin of which is fixed to the mass centre of gravity, the added mass and the damping coefficients were transferred to $O^i x^i y^i z^i$ considering the distance between the water plane and the centre of gravity. The surge added mass for both models is taken to be 5% of the total mass of the model.

The striking model, equipped with a rigid bulb, hit the struck model at a location where a block of soft foam was installed. The structural response in these model-scale experiments was scaled so as to be similar to that in the large-scale ones. The scaling is described in the next section.

Two separate measuring systems were used in the experiments, one to record the ship motions and the other to measure the contact forces in the longitudinal and the transverse directions with respect to the striking ship. The motions were measured with the Rodym DMM noncontact measurement system with a sampling rate of 125 Hz. This system provided the position and the orientation of the models with respect to the inertial frame $O^0 x^0 y^0 z^0$. Taking the time derivatives of the position and the orientation signals yielded velocities in the inertial coordinate system, and the values in the local frames were obtained using Euler's angles, as given by Eqs. 2 and 4. It was estimated that the positions of the models were measured with a precision of ±0.05 mm and their orientations with a precision of ±0.5°.

Two contact force components were measured in the striking ship: the longitudinal force $F^A_{C,x}$ and the transverse force $F^A_{C,y}$. The vertical contact force was not measured because of the limitations of the measuring instrumentation. However, with the contact point being close to the waterline, only small vertical forces were expected. The sampling rate was 1250 Hz and the precision of the measured forces was estimated to be ±0.01 N. The synchronisation of the force and the motion measurements in the time domain is described in Tabri et al. [10].

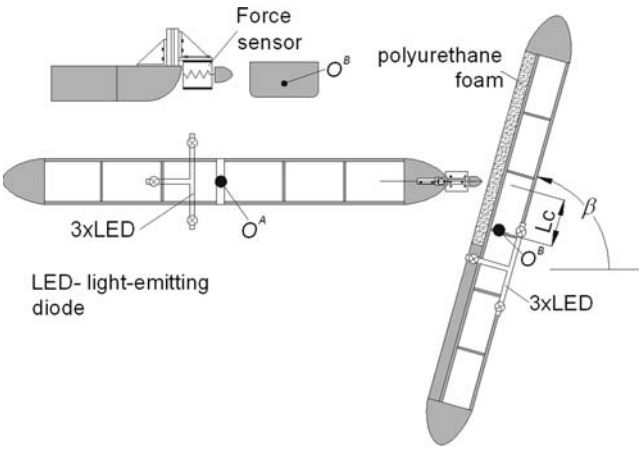

Fig. 4 General arrangements of the model tests

3.2 Force response

The model-scale experiments concentrated on the external dynamics, and the precise deformation mechanics of the side structures were beyond their scope. However, in order

Table 1 Physical parameters of the models

Model	Draft (cm)	Mass (kg)	KG (cm)	k_{XX} (cm)	k_{YY} (cm)	k^a_{ZZ} (cm)	μ_{sway} (%)	μ_{heave} (%)	μ_{roll} (%)	μ_{pitch} (%)	μ_{yaw} (%)
Striking	4	20.5	7.4	19	70	70	17	300	12	220	14
Striking	6	28.5	6.4	15	67	67	23	210	11	170	20
Striking	8	40.5	5.1	9	65	65	28	170	23	146	27
Struck	4	20.5	7.4	19	77	77	16	376	20	231	10
Struck	6	30.5	7.3	17	69	69	21	238	14	184	17
Struck	8	44.5	5.1	9	65	65	27	190	36	164	25

[a] It is assumed that $k_{ZZ} = k_{YY}$

to maintain dynamic similarity, the structural resistance has to be similar to that of the full-scale ship structures. As the properties of the polyurethane foam used as the side structure of the struck model are constant, the level of the contact force can only be modified by changing the shape of the impact bulb. In a preliminary material study, a number of penetration tests were carried out in order to study the crushing mechanisms of the foam [20]. The crushing strength of the foam is assumed to be equal to the stress σ_n at the contact interface and it was determined to be $\sigma_n = 0.121$ MPa. The friction coefficient between the foam and the painted surface of the bulb was $\mu_q = 0.15-0.2$ [20]. Three different axisymmetric bulb shapes presented in Fig. 5 were evaluated [20]. The shapes of the bulbs were defined as an elliptical paraboloid

$$x^A = f^A(a, b, c, y^A, z^A) = -\left(\frac{(y^A)^2}{a^2} + \frac{(z^A)^2}{b^2} + c\right) \tag{35}$$

with the semi-axes a and b having the following values:

$a = b = 0.129$ $[\sqrt{m}]$ for bulb 1;
$a = b = 0.258$ $[\sqrt{m}]$ for bulb 2;
$a = b = 0.169$ $[\sqrt{m}]$ for bulb 3.

Parameter c describes the coordinate value in $O^A x^A y^A z^A$, where the surface of the bulb intersects with the x^A axis and $c = -L^A/2$ as the centre of gravity of the ship was at the amidships.

The force–penetration curve of bulb 1 corresponds well to the X-core large-scale experiment, as seen in Fig. 6. The thick line presents the large-scale measurement [10, 21], which is scaled down with a scaling factor of $\lambda = 35$. The thin line is measured from the model-scale test with bulb 1, and the dashed line is obtained using the approach presented in Sect. 2.3. The other two bulbs provided significantly higher resistance compared to that of the large-scale experiment. It should however be noted that such a presentation of structural resistance is very general, and only presents realistic structural behaviour to a certain extent. With extensive deformations, the actual force–penetration curve could be different from the monotonously increasing curve of the current setup. However, the approach is still valuable due to its simplicity and is sufficient to maintain the physical similarity with respect to the external dynamics.

In the time simulations of the collision experiments, the recovered shape of the deformed foam was evaluated on the basis of the shape of the impacting bulb, the relative thickness of the recovered region ε, and the maximum translational penetration $\boldsymbol{\delta}^0 \cdot \mathbf{j}^B$ in the struck ship. With the point of contact located in the parallel middle body, the struck ship can be presented as a plane in $O^A x^A y^A z^A$:

$$x^A = -\left(Ay^A + Bz^A + C\right) \tag{36}$$

The parameters A, B, and C depend on the current position and on the orientation of the struck ship. Given definitions for the geometries of the ships (Eqs. 35 and 36), the penetration depth $\boldsymbol{\delta}^0$ can be evaluated, and thus, based on Eq. 26, the shape of the recovered region in $O^A x^A y^A z^A$ is written as

$$\begin{aligned} x^A &= f^{\varepsilon}\left(a, b, c, \varepsilon, \boldsymbol{\delta}^0 \cdot \mathbf{j}^B, y^A, z^A\right) \\ &= -\left(\frac{(y^A)^2}{[(1-\varepsilon)a]^2} + \frac{(z^A)^2}{[(1-\varepsilon)b]^2} + c - \varepsilon\left(\boldsymbol{\delta}^0 \cdot \mathbf{j}^B\right)\right) \end{aligned} \tag{37}$$

Upon comparing the experimentally measured force–penetration curves to those evaluated with the approach presented in Sect. 2.3, the relative thickness of the recovered region ε was determined to be around $\varepsilon = 0.03$.

3.3 Test matrix

The model-scale experiments were divided into three different sets on the basis of the type of collision scenario.

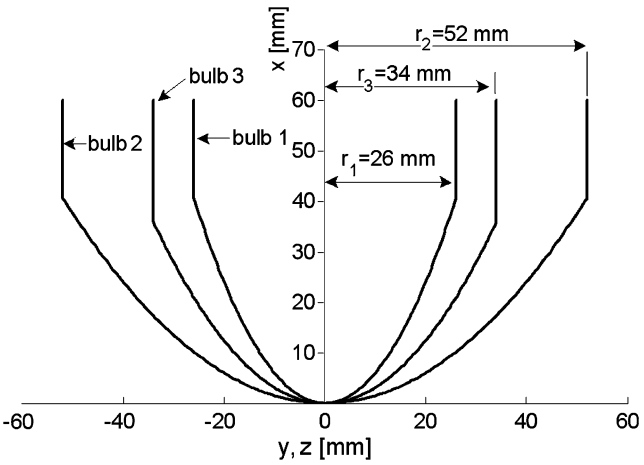

Fig. 5 Geometries of the axisymmetric impact bulbs used in the model-scale experiments

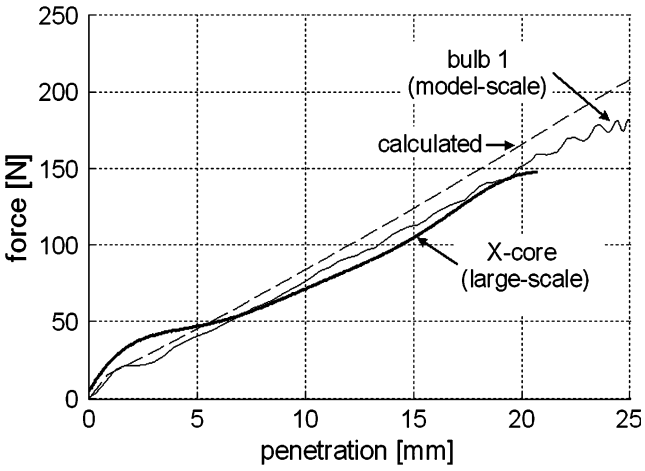

Fig. 6 Force–penetration curves obtained in the large- and the model-scale experiments and by calculations. Large-scale measurements are scaled to the model scale with $\lambda = 35$

The first set concentrated on symmetric collisions and is not discussed here. The second and the third sets consisted of nonsymmetric collision experiments. In the second set, the location of the contact point was changed, ranging from an eccentricity of $0.13L^B$ (30 cm) to $0.36L^B$ (83 cm) from the amidships towards the bow, but the collision angle β was still 90°. The motions of the striking ship were mainly translational, while the struck ship was subject to yaw motions in addition to translations. In the third set, the collision angles varied from 30° to 120° and the eccentricity was around $\sim 0.18L^B$ ($\sim$40 cm). The yaw motions of both ships were significant, yielding diverse motion dynamics. The complete test matrix containing the experiments in the second and third sets is presented in Appendix 2.

4 Validation

The model-scale experiments provided a vast amount of data for the validation. Here, this amount is limited to a set sufficient to provide qualitative and quantitative validation. Four experiments presenting distinctively different collision scenarios were chosen for thorough analysis: test 202 from the second set, and tests 301, 309, and 313 from the third set. Test 202 was a collision at right angles with an eccentricity of $0.36L^B$ (83 cm). In tests 301, 309, and 313, the eccentricity was about $0.16L^B - 0.19L^B$ (37–44 cm) and the collision angles were 120°, 145°, and 60°, respectively. More detailed information about the selected experiments is presented in Appendix 2.

The time histories of the calculated and the measured longitudinal contact force $F^A_{C,x}$ and the transverse contact force $F^A_{C,y}$ as experienced by the striking ship are presented in Fig. 7. In addition to the measured forces, the calculated time history of the vertical contact force $F^A_{C,z}$ is also given in the figure. In test 202, the longitudinal force is clearly dominant and only a minor transverse force arises as a result of the yawing of the struck ship. The transverse force increases significantly when the collision angle is other than 90°. In tests 301 and 313, the transverse force changes its direction as the bow gets stuck in the foam. With the large collision angle in test 309, the bow slides along the struck ship and the transverse force remains positive throughout the contact. The calculations predict the loading phase well; the deviation from the measurements increases in the unloading phase. This consists of more complicated mechanisms, which cannot be precisely predicted with robust calculation models. In the calculations, the stiction phase appears as a somewhat unrealistic drop in the force values. The stiction phase can clearly be seen in test 202 at $t = \sim 55$ ms. When the stiction is not considered in the

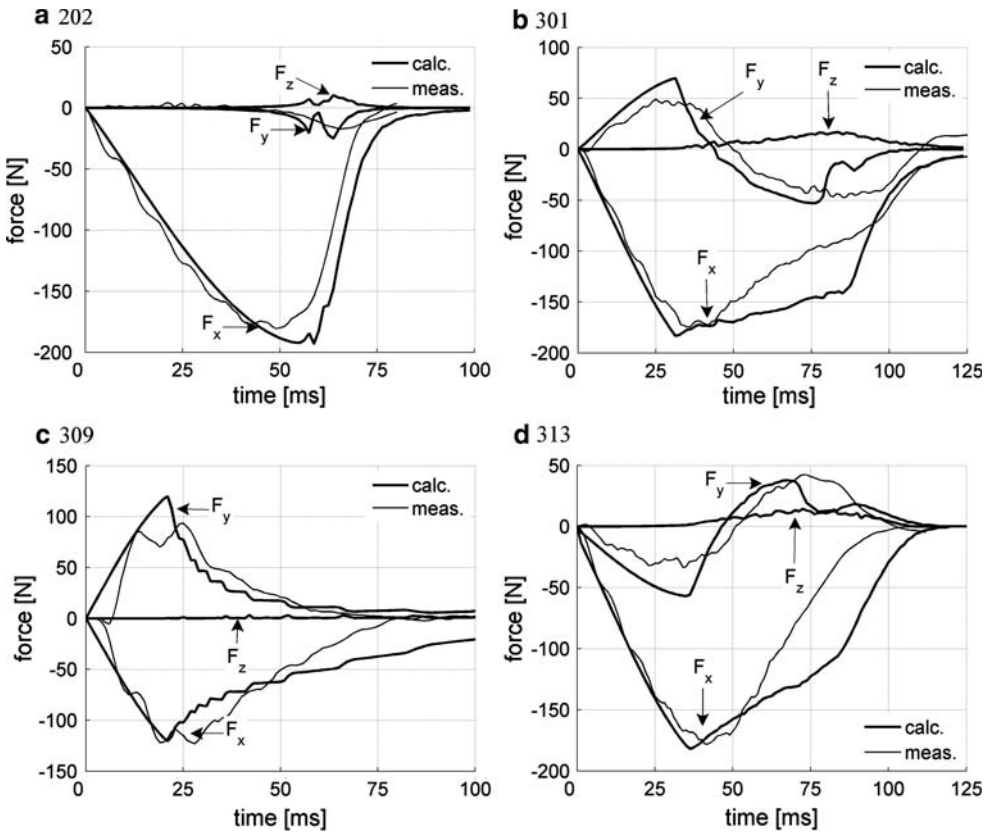

Fig. 7 Calculated and measured components of the contact force $\mathbf{F}^A_C$ as experienced by the striking ship (superscript A and subscript C are omitted for brevity)

calculations, the drop in the force value is more significant and has a longer duration, as shown in Fig. 8, which presents two calculations of $F^A_{C,x}$ in test 202, one with stiction included and the other without.

The calculated vertical contact force is clearly lower than the other force components. Even though minor rolling of the struck ship occurs in the calculations, the distribution of the contact pressure in the vertical direction is rather symmetric, and thus the resultant force becomes low.

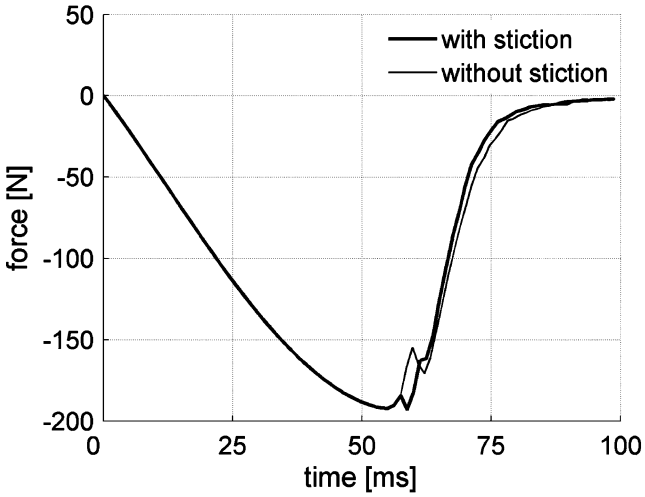

Fig. 8 Calculated contact force $F^A_{C,x}$ with and without stiction phase included (test 202)

The motions of the ships are presented in Fig. 9 as the position of the origin O^i in the inertial frame. Their positions are scaled to start from zero. A circular marker is drawn every 20 ms to include the time scale. Displacement along the x^0 axis is an order of magnitude larger compared to the y^0 displacement. This is to be expected, as the initial velocity of the striking ship was along the x^0 axis. Displacement along the x^0 axis is predicted well in terms of both distance and time. In the transverse direction the relative differences are larger, but are acceptable, considering their small magnitude.

The yaw angle of the struck ship is presented in Fig. 10. The magnitude of the angle at the end of the contact is about 1°, but it is still very important for evaluating the penetration history. The yaw is the largest in test 202, as a result of the high eccentricity. The calculation model tends to somewhat underestimate the angular motions.

Considering the position and the orientation of the models, the bulb's penetration paths can be evaluated. Figure 11 presents the path of the tip of the penetrating bulb inside the side structure of the struck ship. In test 202 the penetration has almost only the transverse component. During the short transient contact phase, the angular motions of the ships are still too small to extend the

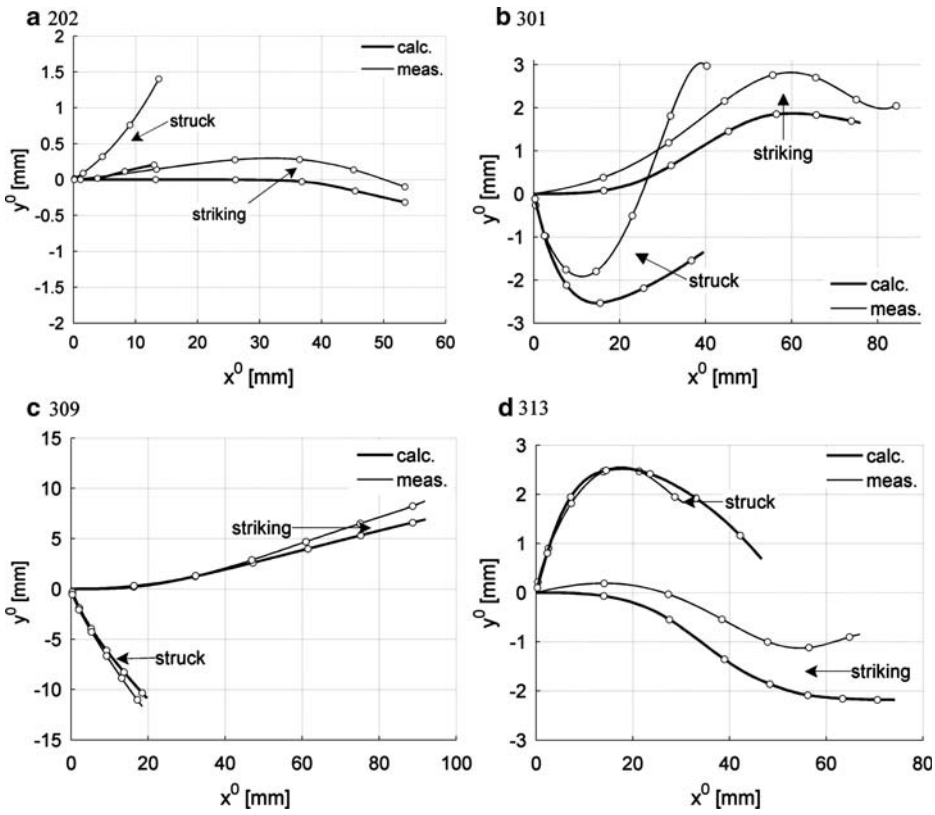

Fig. 9 Position of O^i in the inertial frame (marker spacing 20 ms). Note the different scales of the y^0 axis

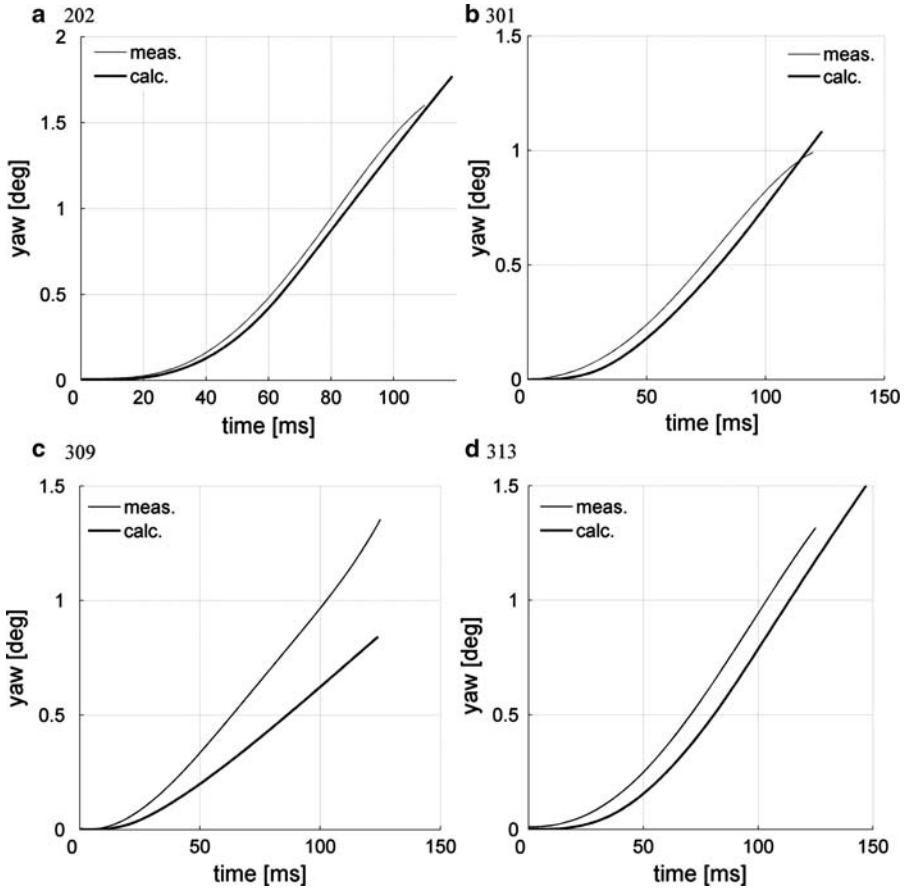

Fig. 10 Yaw angle of the struck ship

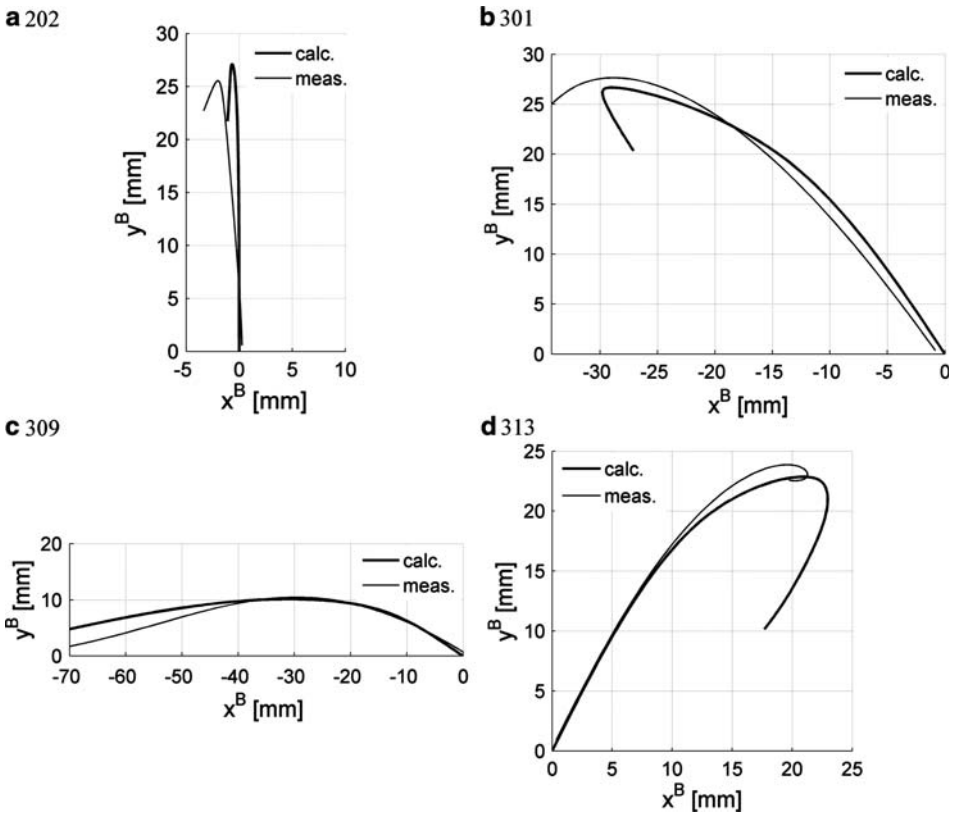

Fig. 11 Penetration paths of the bulb in the struck ship

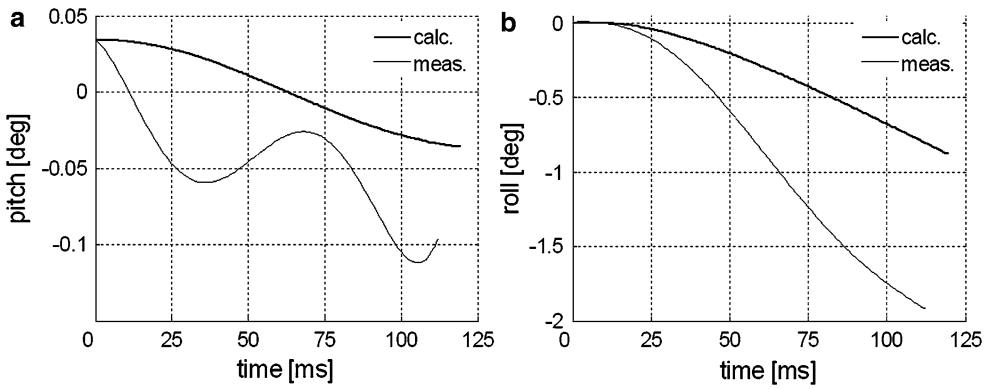

Fig. 12 Pitch of the striking ship (**a**) and roll of the struck ship (**b**)

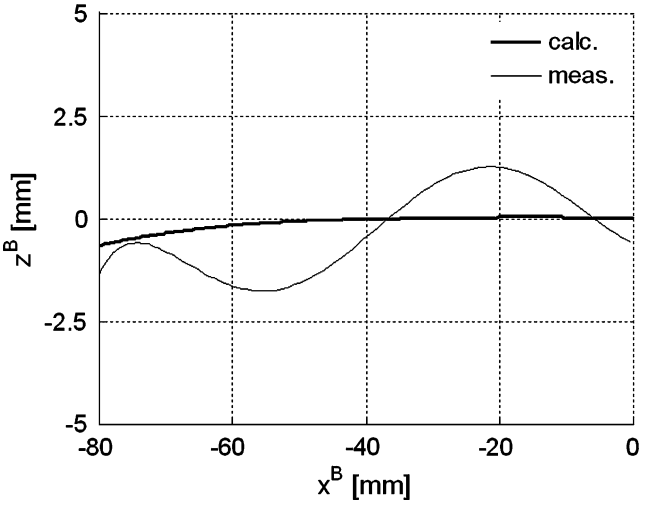

Fig. 13 Penetration in the vertical direction in test 309. Note the scaled z^B axis

penetration in other directions. Test 309 presents an opposite scenario, in which the striking ship slides along the side of the struck ship, causing shallow but long penetration. The penetrations in tests 301 and 313 extend almost equally in both directions. While in the other tests the calculation model predicted the penetration paths well, in test 313 the penetration in the longitudinal direction is underestimated.

The above analysis focused on the motions in the plane of the water surface. When looking at the other motion components, such as the rolling of the struck ship and the pitching of the striking ship, the calculation model misses the effects arising from the waves generated by the moving ships. This situation is analysed by looking at the results of test 309, where these effects were clearly present. The calculation model considers only the roll and the pitch caused by the vertical and the horizontal eccentricity between the contact point and the centre of gravity. However, the measured angular motions clearly exceed these values, as shown in Fig. 12. As a consequence, the penetration in a vertical direction is also underestimated in the calculations; see Fig. 13. Some conclusions can be drawn on the basis of the visual analysis of the videos of the model-scale experiments. In these, the pitching of the striking ship is due to the wave trough left behind by the accelerating struck ship, and (through the contact between the ships) this also increases the rolling of the struck ship.

5 Conclusions

The developed calculation model predicts the motions and the forces in the plane of the water surface rather accurately. The character of the contact forces is highly dependent on the collision scenario, i.e. on the exact angle and location of the collision. In an eccentric collision at right angles, the contact force, and thus also the penetration, is transverse to the struck ship and has only a minor longitudinal component. In collisions at small or large angles, the extent of the damage to the side of the struck ship is long and shallow. In all of the calculated scenarios the forces are predicted well in the loading stage, while during the unloading some deviations from the measurements occur. This, as well as a somewhat unrealistic and rapid drop in the force values in the stiction phase, indicates that the interaction model cannot fully describe these complex phenomena. However, these effects are small when looking at the penetrations.

The longitudinal and the transverse penetration inside the struck ship are properly predicted with the calculation model, while they are slightly underestimated in the vertical direction. This is due to the pitching of the striking ship, as induced by complex wave patterns during the collision. The effect of this is not considered in the calculation model. This hydrodynamic interaction as well as the effect of the forward speed of the struck ship is left for future studies.

The model for evaluating the contact force could be extended to consider ship-like side structures whose deformation mechanisms are extremely complex in comparison to that of the side structure used in the model-scale experiments. This, together with motion simulations, would

improve the accuracy of collision analyses and thus allow the crashworthinesses of different structural arrangements to be enhanced.

Appendix 1: Scalar form of equations of motion

For numerical integration, the equation of motion

$$\begin{bmatrix} [\mathbf{M}] & 0 \\ 0 & [\mathbf{I}] \end{bmatrix} \begin{Bmatrix} \dot{\mathbf{u}} \\ \dot{\Omega} \end{Bmatrix} + \begin{Bmatrix} [\mathbf{M}]\boldsymbol{\Omega} \times \mathbf{u} \\ \boldsymbol{\Omega} \times [\mathbf{I}]\boldsymbol{\Omega} \end{Bmatrix} - \mathbf{F}_{\mathrm{R}} - \mathbf{F}_{\mu} = \begin{Bmatrix} \mathbf{F} \\ \mathbf{G} \end{Bmatrix} - \mathbf{F}_{\mathrm{R}} - \mathbf{F}_{\mu} \tag{38}$$

is rearranged to obtain a more convenient form:

$$[\mathbf{M}_{\mu}] \begin{Bmatrix} \dot{\mathbf{u}} \\ \dot{\Omega} \end{Bmatrix} + \left[\mathbf{M}_{\mu}^{\Omega}\right] \begin{Bmatrix} \mathbf{u} \\ \boldsymbol{\Omega} \end{Bmatrix} - \left([\mathbf{T}]^{\mathrm{T}} [\mathbf{K}] \begin{Bmatrix} \mathbf{R} \\ [\boldsymbol{\varphi}] \end{Bmatrix} + [\mathbf{K}] \begin{Bmatrix} \{\mathrm{d}\mathbf{x}\} \\ [\mathrm{d}\boldsymbol{\varphi}] \end{Bmatrix} \right) = \begin{Bmatrix} \mathbf{F} \\ \mathbf{G} \end{Bmatrix} - \mathbf{F}_{\mathrm{R}} - \mathbf{F}_{\mu} \tag{39}$$

where the matrices have the following component form:

$$[\mathbf{M}_{\mu}] = \begin{bmatrix} m+a_x & 0 & 0 & 0 & 0 & 0 \\ 0 & m+a_y & 0 & a_{yx} & 0 & a_{yz} \\ 0 & 0 & m+a_z & 0 & a_{zy} & 0 \\ 0 & a_{xy} & 0 & I_x + a_{xx} & 0 & -I_{xz} \\ 0 & 0 & a_{yz} & 0 & I_y + a_{yy} & 0 \\ 0 & a_{zy} & 0 & -I_{xz} & 0 & I_x + a_{zz} \end{bmatrix}, \tag{40}$$

$$\left[\mathbf{M}_{\mu}^{\Omega}\right] = \begin{bmatrix} 0 & -(m+a_x)r & (m+a_x)q & 0 & 0 & 0 \\ (m+a_y)r & 0 & -(m+a_y)p & 0 & 0 & 0 \\ -(m+a_z)q & (m+a_z)p & 0 & 0 & 0 & 0 \\ 0 & 0 & 0 & 0 & I_{45} & -I_{46} \\ 0 & 0 & 0 & -I_{45} & 0 & I_{56} \\ 0 & 0 & 0 & I_{46} & -I_{56} & 0 \end{bmatrix} \tag{41}$$

with

$$I_{45} = (I_{zz} + a_{zz})r - (I_{zx} + a_{zx})p - I_{zy}q,$$
$$I_{46} = (I_{yy} + a_{yy})q - I_{yz}r - I_{yx}p,$$
$$I_{56} = I_{xx} + a_{xx}p - I_{xy}q - I_{xz} + a_{xz}r$$

and

$$[\mathbf{K}] = \begin{bmatrix} 0 & 0 & 0 & 0 & 0 & 0 \\ 0 & 0 & 0 & 0 & 0 & 0 \\ 0 & 0 & -\rho g A_W & 0 & \rho g A_W x_F & 0 \\ 0 & 0 & 0 & -GM_{\mathrm{T}} g m & 0 & 0 \\ 0 & 0 & \rho g A_W x_F & 0 & -GM_{\mathrm{L}} g m & 0 \\ 0 & 0 & 0 & 0 & 0 & 0 \end{bmatrix}$$

where m is the structural mass, a_i and a_{ii} are the translational and rotational added masses, A_W is the waterplane area, x_F is the longitudinal centre of flotation, ρ is the water density, g is the gravitational acceleration, GM_{T} is the transverse metacentric height, and GM_{L} is the longitudinal metacentric height. The subscript characters in the mass and inertia terms follow the common notation; a single character refers to a value involved with translational motions, and two characters refer to rotational motion or to a coupling between two motion components.

The restoring force is divided into a constant part $\mathbf{F}_{\mathrm{R}}|_{t_j}$ evaluated at the beginning of the time increment at $t = t_j$, and into the change $\mathrm{d}\mathbf{F}_{\mathrm{R}}|_{t_{j+1}}$ in the force during the increment:

$$\mathbf{F}_{\mathrm{R}}|_{t_j} + \mathrm{d}\mathbf{F}_{\mathrm{R}}|_{t_{j+1}} = [\mathbf{T}]^{T} [\mathbf{K}] \begin{Bmatrix} \mathbf{R} \\ [\boldsymbol{\varphi}] \end{Bmatrix} + [\mathbf{K}] \begin{Bmatrix} \{\mathrm{d}\mathbf{x}\} \\ [\mathrm{d}\boldsymbol{\varphi}] \end{Bmatrix} \tag{42}$$

This split is necessary, as the restoring force depends on the ship's position with respect to the inertial coordinate system given by the position vector $\mathbf{R}$ and Euler's angles. The increase in the force during the time increment is still evaluated via the displacements in the local coordinate system, but because of small angular displacements the error will be negligible.

During the time increment, the matrices and vectors on the left-hand side of Eq. 39 are updated several times within the increment, while the right-hand side is kept constant.

Appendix 2: Test matrix for second and third sets

Test	β (deg)	Bulb	L_C (m)	m^A (kg)	m^B (kg)	u_0 (m/s)	$F^A_{\mathrm{C},x}$ (N)	$F^A_{\mathrm{C},y}$ (N)	$E_{\mathrm{D,P}}$ (J)
201	90	1	0.82	28.5	30.5	0.87	226	25	3.91
202	90	1	0.83	28.5	30.5	0.71	179	17	2.36
203	90	1	0.83	28.5	30.5	0.38	91	13	0.75
204	90	1	0.45	28.5	30.5	0.91	300	36	6.30
205	90	1	0.48	28.5	30.5	0.38	115	6	0.95
206	90	1	0.38	28.5	30.5	0.71	221	13	3.43
207	90	1	0.80	28.5	20.5	0.90	200	27	4.2
208	90	1	0.41	28.5	20.5	0.89	229	33	4.92
301	120	1	0.37	28.5	20.5	0.87	172	47	4.20
302	120	1	0.32	28.5	20.5	0.30	59	14	0.51
303	120	1	0.3	28.5	44.5	0.84	204	52	6.50
304	120	1	0.38	28.5	44.5	0.37	89	21	1.01
305 (sliding)	145	1	0.32	28.5	20.5	0.34	44	29	0.54
306 (sliding)	145	1	0.44	28.5	20.5	0.87	115	65	3.91
307 (sliding)	145	1	0.38	28.5	44.5	0.84	118	67	5.47
308	145	1	0.34	28.5	44.5	0.28	45	27	0.52
309 (sliding)	145	3	0.46	28.5	20.5	0.87	120	86	3.19
310 (sliding)	145	2	0.44	28.5	20.5	0.88	142	94	3.19
311	120	3	0.42	28.5	20.5	0.88	217	69	4.25
312	120	2	0.41	28.5	20.5	0.86	313	104	4.64
313	60	1	0.29	28.5	20.5	0.76	177	41	3.14
314	60	1	0.32	28.5	20.5	0.36	80	16	0.81
315	60	1	0.38	28.5	44.5	0.75	202	52	4.35
316	60	1	0.4	28.5	44.5	0.43	104	24	1.17

Absolute maximum values are presented for $F^A_{\mathrm{C},x}$ and $F^A_{\mathrm{C},y}$

m, ship mass; u^0, contact velocity; $E_{\mathrm{D,P}}$, plastic deformation energy

References

1. Eliopoulou E, Papanikolaou A (2007) Casualty analysis of large tankers. J Mar Sci Technol 12:240–250
2. Tuovinen J (2005) Statistical analysis of ship collisions (master's thesis). Helsinki University of Technology, Helsinki
3. Minorsky VU (1959) An analysis of ship collision with reference to protection of nuclear power plants. J Ship Res 3:1–4
4. Woisin G (1988) Instantaneous loss of energy with unsymmetrical ship collisions. Schiff Hafen 40:50–55
5. Pedersen PT, Zhang S (1998) On impact mechanics in ship collisions. J Mar Struct 11:429–449
6. Petersen MJ (1982) Dynamics of ship collisions. Ocean Eng 9:295–329
7. Brown AJ (2002) Collision scenarios and probabilistic collision damage. J Mar Struct 15:335–364
8. Cummins WE (1962) The impulse response function and ship motions. Schifftechnik 9:101–109
9. Ogilvie TF (1964) Recent programme towards the understanding and prediction of ship motions. In: Proceeding 5th Symp on Naval Hydrodynamics, Bergen, Norway, 10–12 Sept 1964, pp 3–128
10. Tabri K, Määttänen J, Ranta J (2008) Model-scale experiments of symmetric ship collisions. J Mar Sci Technol 13:71–84
11. Clayton BR, Bishop RED (1982) Mechanics of marine vehicles. E. F. N. Spon Ltd, London
12. Gale C, Eronen H, Hellevaara M, Skogman A (1994) Perceived advantages of Z-drive escort tugs. In: Proceeding Int Towage and Salvage Convention, Southampton, UK, 17–21 Oct 1994, pp 163–176
13. Matusiak J (2001) Importance of memory effect for ship capsizing prediction. In: Proceeding 5th Int Workshop on Ship Stability, Trieste, Italy, 12–13 Sept 2001
14. Dupont P, Armstrong B, Hayward V (2000) Elasto-plastic friction model: contact compliance and stiction. In: Proceedings of the American Control Conference. AACC, Chicago, pp 1072–1077
15. Canudas de Wit C, Olsson H, Åström J, Lischinsky P (1995) A new model for control of systems with friction. IEEE Trans Automat Contr 40:419–425
16. Dormand JR, Prince PJ (1980) A family of embedded Runge–Kutta formulae. J Comp Appl Math 6:19–26
17. Wevers LJ, Vredeveldt AW (1999) Full scale ship collision experiments (TNO report 98-CMC-R1725). TNO, Delft
18. Määttänen J (2005) Experiments on ship collisions in model scale (master's thesis). Helsinki University of Technology, Helsinki
19. Journée JMJ (1992) Strip theory algorithms (report MEMT 24). Delft University of Technology, Delft
20. Ranta J, Tabri K (2007) Study on the properties of polyurethane foam for model-scale ship collision experiments (report M-297). Helsinki University of Technology, Helsinki
21. Tabri K, Broekhuijsen J, Matusiak J, Varsta P (2009) Analytical modelling of ship collision based on full-scale experiments. J Mar Struct 22:42–61